ELSEVIER

Coordination Chemistry Reviews
200–202 (2000) 349–377

COORDINATION CHEMISTRY REVIEWS

www.elsevier.com/locate/ccr

Coordination chemistry with *meso*-hydroxylated porphyrins (oxophlorins), intermediates in heme degradation

Alan L. Balch *

Department of Chemistry, University of California, Davis, CA 95616, USA

Received 1 September 1999; accepted 7 January 2000

Contents

Abstract

An overview of the chemistry of *meso*-hydroxylated porphyrins or oxophlorins is presented with emphasis on the relevance to their occurrence as intermediates in heme degradation.

Keywords: Coordination chemistry; Porphyrins (oxophlorins); Heme degradation; Iron

* Tel.: +1-530-752 0941; fax: +1-530-752 8995.
E-mail address: albalch@ucdavis.edu (A.L. Balch).

0010-8545/00/$ - see front matter
PII: S0010-8545(00)00258-7

1. Introduction

The coordination chemistry of metalloporphyrins has been extensively investigated in order to understand the ability of this macrocycle to sustain a variety of biological functions including dioxygen transport and storage, peroxide disproportionation and oxidative utilization, substrate oxidation, and electron transport [1]. Covalent modification of the porphyrin core can produce significant alterations in the properties of the basic macrocycle. This review is concerned with the coordination chemistry of porphyrins that have been modified by the presence of a hydroxyl group at a *meso* position. The resulting macrocycles can exist in two principle tautomeric forms, the *meso*-hydroxyporphyrin, **1a**, and the oxophlorin, **1b**.

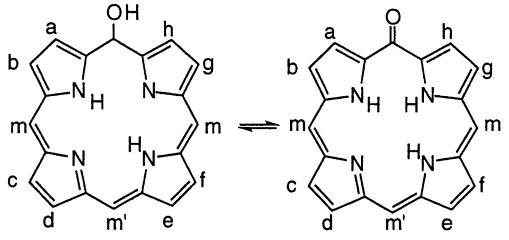

1a **1b**

This relatively modest change to the ligand core results in a tetrapyrrole ligand that is more readily oxidized than its porphyrin counterpart. The essential organic chemistry of this class of tetrapyrrole has been treated in a review [2]. Naturally **1** should be capable of binding metal ions and a number of early reports described the formation of metal complexes [3,4]. The tetrapyrrole **1** is subject to facile oxidation and the formation of free radicals from the hydroxyheme, **1**, has been known for sometime [5–7]. As a ligand, tetrapyrrole **1** should be viewed as part of a three-membered electron transfer series as seen in Scheme 1 where only one of several resonance structures and tautomeric forms for each oxidation state is shown. Biologically, the *meso*-hydroxylated porphyrins are significant in the process of heme cleavage by heme oxygenase as shown in Scheme 2 [8–14]. In this

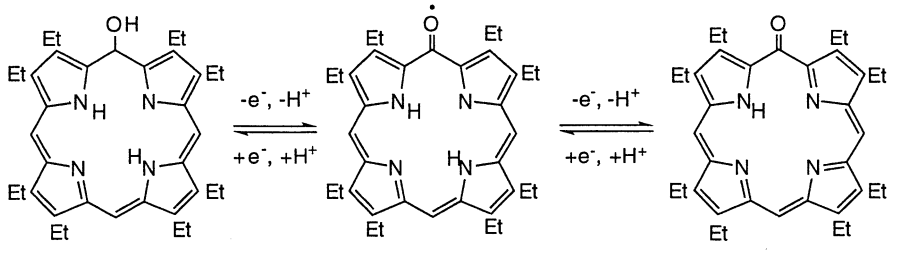

Scheme 1.

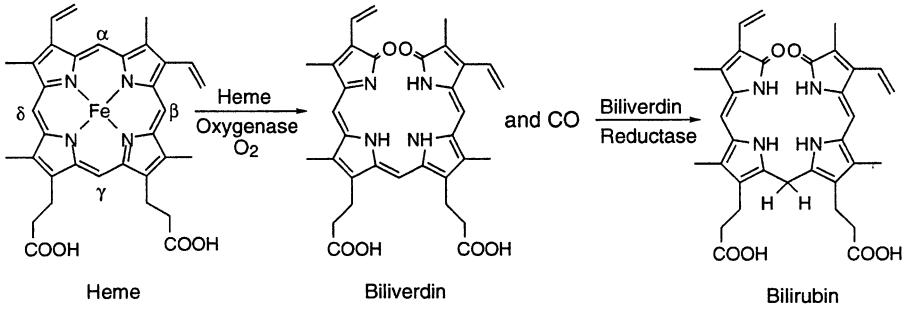

Scheme 2. Biological heme degradation.

reaction heme is a substrate which also activates dioxygen to attack the macrocycle and to open the porphyrin. Biliverdin, carbon monoxide (a potential neurotransmitter), and free iron ions are the products of the reaction. An early step in the heme/heme oxygenase/dioxygen reaction produces regiospecific hydroxylation of the heme at the α-*meso* site. Accounting for the nature of the active oxidant and the cause of the regiospecificity of this step represents a major challenge to our understanding of heme oxygenase.

2. Overview of coordination modes

Scheme 3 presents a synopsis of the major structural forms that have been encountered to date in metal complexes of the *meso*-hydroxylated hemes. Four basic modes of coordination have been characterized. These include: **2** with coordination in a porphyrin-like mode as a dianion with a simple *meso*-hydroxyl group, **3** with coordination in a dimeric fashion as a trianion with the *meso* phenoxide-like units acting as bridges to the adjacent macrocycle, **4** with coordination as an oxophlorin trianion, and finally **5** with coordination as a dianionic, ligand-based free radical. Stable examples of each structural type have been isolated and characterized by single crystal X-ray diffraction as well as by UV–vis, infrared, and ^{1}H NMR spectroscopy. The bulk of this work has involved the symmetric ligand, H_2OEPOH, **1** with a–h = C_2H_5, which is readily obtained by oxidation of commercially available octaethylporphyrin [15].

3. Monomeric complexes with *meso*-hydroxyl groups

The structure of the prototypical example of a complex of this type, {(py)Zn^{II}(OEPOH···py)}, is shown in Fig. 1 [16]. The complex contains two pyridine molecules. One is coordinated to the zinc ion, which is five-coordinate, while the other is hydrogen bonded to the *meso*-hydroxyl group. This hydrogen bond is especially important because it emphasizes the location of the hydroxyl

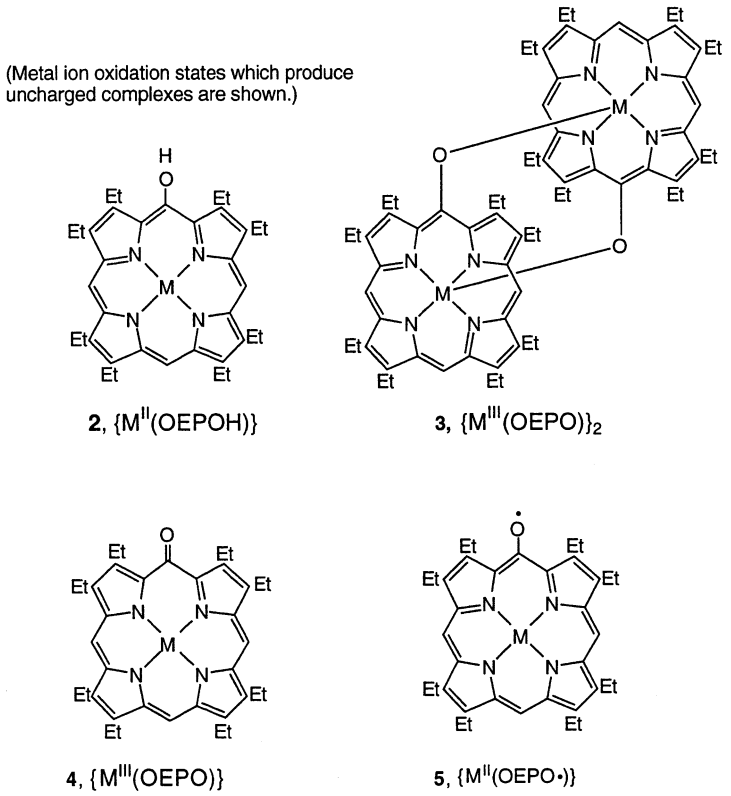

Scheme 3. Basic types of coordination. (Metal ion oxidation states which produce uncharged complexes are shown.)

group and is responsible for producing an ordered structure with the hydroxyl group confined to a specific site within the crystal lattice. The ^{1}H NMR spectrum of the complex shows a characteristic resonance at 13.4 ppm in pyridine-d_5 for the *meso*-hydroxyl proton.

A similar structure has been crystallographically determined for the low-spin ($S = 1/2$) cobalt(II) complex, {(py)Co^{II}(OEPOH···py)} [17]. Both of these five-coordinated complexes, {(py)Zn^{II}(OEPOH···py)} and {(py)Co^{II}(OEPOH···py)}, are sensitive to aerial oxidation, and the products of their oxidation will be discussed in Sections 5 and 6.

Fig. 2 shows the structure of four-coordinate, diamagnetic {Ni^{II}(OEPOH)} [8]. This structure demonstrates a commonly encountered problem, disorder in the location of the unique *meso* substituent, in the structures of complexes obtained from H_2OEBOH. The *meso* substituent, either a hydroxyl group or keto group, is effectively buried between the adjacent ethyl groups and does not necessarily to contribute to the external shape of the complex. Hence, this group has little influence on the orientation of the complex within the crystal. Consequently,

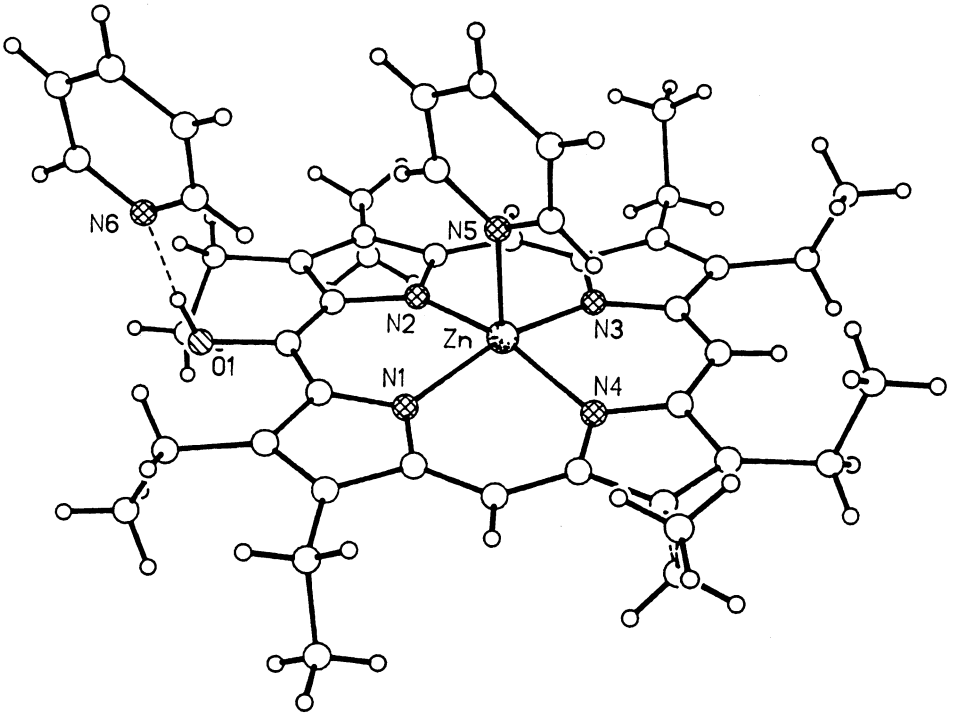

Fig. 1. The crystallographically determined structure of {(py)Zn^{II}(OEPOH···py)}. The in-plane Zn–N distances are: N1, 2.093(9); N2, 2.064(8); N3, 2.060(9); and N4, 2.099(8) while the Zn–N5 distance is 2.183(8) Å. Taken from Balch et al. [16].

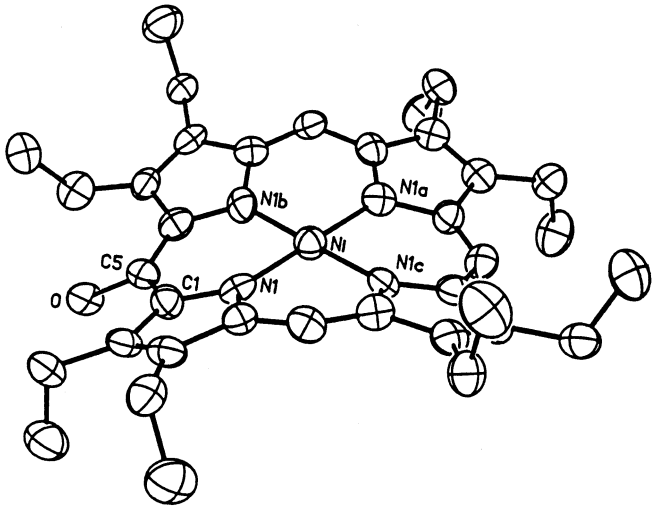

Fig. 2. A drawing of the crystallographically determined structure of {Ni^{II}(OEPOH)} (with 50% thermal contours), which has crystallographically imposed *S*4 symmetry. There is disorder in the location of the *meso*-hydroxyl group and only one of the four, equally occupied sites is shown. Taken from Balch et al. [18].

disorder is common, unless an additional feature, such as the hydrogen bond seen for {(py)Zn^{II}(OEPOH···py)} in Fig. 1, is present. The nickel atom resides on an S_4 axis, and the *meso*-hydroxyl group is equally disordered over all for *meso* positions. The macrocycle is also strongly distorted from planarity into a saddle shape about the S_4 axis. Thus complexes that contain the tautomeric form, **1a**, can undergo distortions from planarity in a manner entirely analogous to the distortions found with porphyrins [19].

The complexes with *meso*-hydroxyl groups discussed in this section should undergo acid/base reactions in which the hydroxyl group is deprotonated. To date, no complex of this type appears to have been thoroughly structurally characterized, however there is spectroscopic evidence that complexes of type **2** do undergo deprotonation [3].

4. Dimeric complexes with *meso*-phenoxide-like bridges

Fig. 3 shows the structure of the dimeric complex, $\{In^{III}(OEPO)\}_2$ [20]. In this molecule the two porphyrin units are held in close, face-to-face proximity by the phenoxide-like bridges. This arrangement is facilitated by the five-coordinate indium atom which extends out away from the N_4 coordination plane and by bending of the *meso* oxygen atom out of the plane of the two adjacent pyrrole rings. This dimer serves as an appropriate structural model for the three other dimeric complexes, $\{Fe^{III}(OEPO)\}_2$ [21,22], $\{Mn^{III}(OEPO)\}_2$ [23], and $\{Ga^{III}(OEPO)\}_2$ [24], that have been isolated. The magnetic properties of the dimers indicate that both $\{Fe^{III}(OEPO)\}_2$ and $\{Mn^{III}(OEPO)\}_2$ contain high-spin ions which are weakly antiferromagnetically coupled through the phenoxide-like bridges. The chemistry of $\{Fe^{III}(OEPO)\}_2$ is discussed further in Section 7. It should also be possible to obtain heterodimers with different metal ions in each macrocycle as has been done by Latos-Grażyński with the related, phenoxide-bridged trimers of 2-hydroxy substituted porphyrins [25], but such mixed metal dimers have not as yet been reported. Additionally, it should be possible to use the phenoxide-like group as a bridge to connect the $[M^{II}(OEPO)]^-$ unit to another metal complex.

The availability of axial ligands effects the structural integrity of the these face-to face dimers. Addition of pyridine to $\{M^{III}(OEPO)\}_2$ results in cleavage to form monomers as shown in Scheme 4 [22]. The nature of the products obtained from this type of cleavage are discussed in the next section. Similarly addition of acids, HX, to the dimers results in disruption of the dimers as shown in Scheme 4. In this reaction HX supplies both an axial ligand (X^-) and a proton to add to the phenoxide-like group.

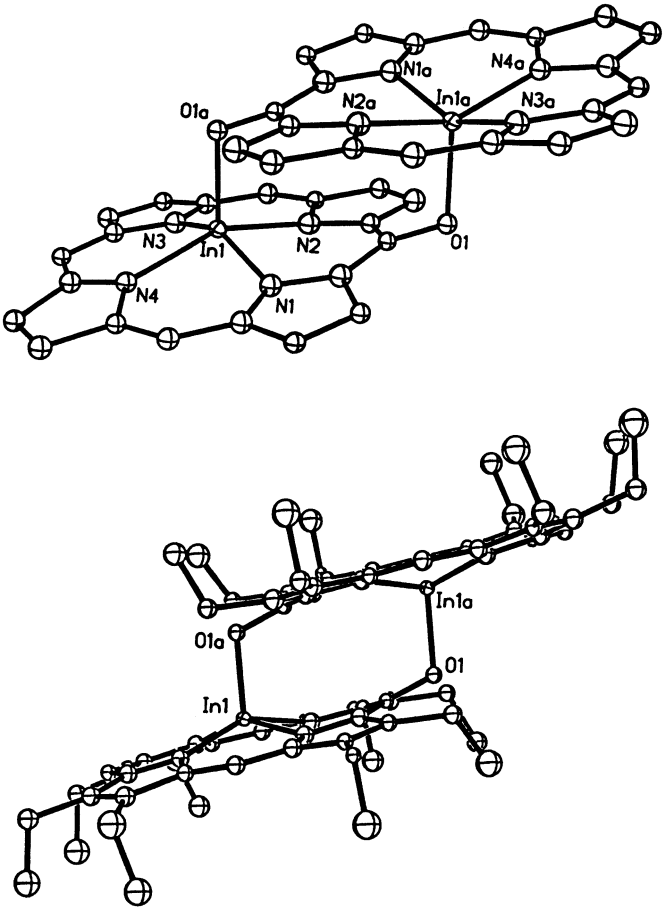

Fig. 3. Two views of the crystallographically determined structure of $\{In^{III}(OEPO)\}_2$ with 50% thermal contours. The top view shows the core of the dimer with the ethyl groups removed for clarity while the bottom view shows the entire molecule from an edge-on perspective that emphasizes the planarity of the macrocyclic ligands. Taken from Balch et al. [20].

5. Coordinated oxophlorin trianions

Cleavage of $\{Mn^{III}(OEPO)\}_2$ by pyridine (Scheme 4) produces orange crystals of $\{(py)_2Mn^{III}(OEPO\}$ whose magnetic moment, 5.2 μB, indicates that it contains a high-spin ($S = 2$) Mn(III) ion [22]. The structure of this monomeric, six-coordinate complex, with the manganese atom on a crystallographic center of symmetry, is shown in Fig. 4. The Mn–N distances (2.022(4) and 2.018(3) Å) for the in-plane pyrrolic nitrogen atoms are shorter than the corresponding distance (2.376(8) Å to the pyridine nitrogen atom. These distances are consistent with the presence of high-spin Mn(III) in which the out-of-plane d_z2 orbital is filled while the in-plane $d_{x^2-y^2}$ orbital is empty. The macrocyclic ligand is planar, but the *meso* oxygen

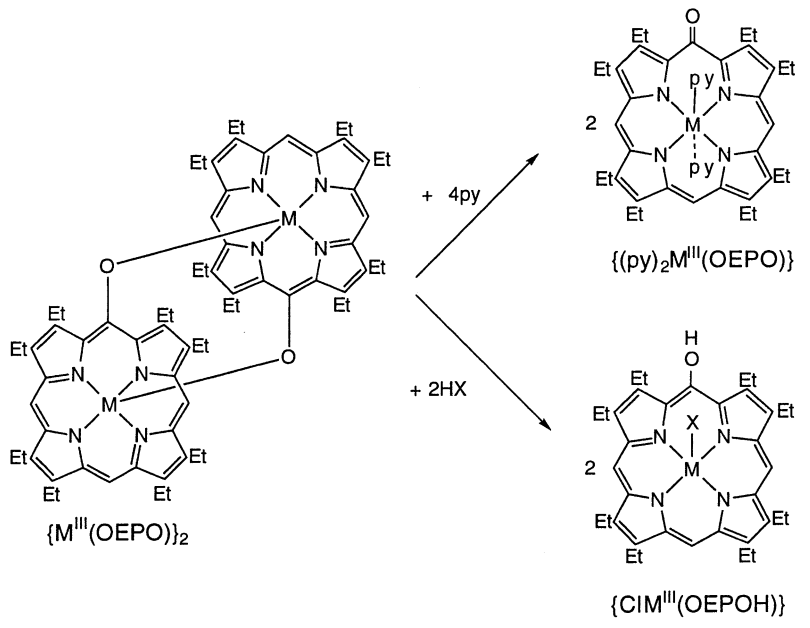

Scheme 4. Cleavage of face-to-face dimers.

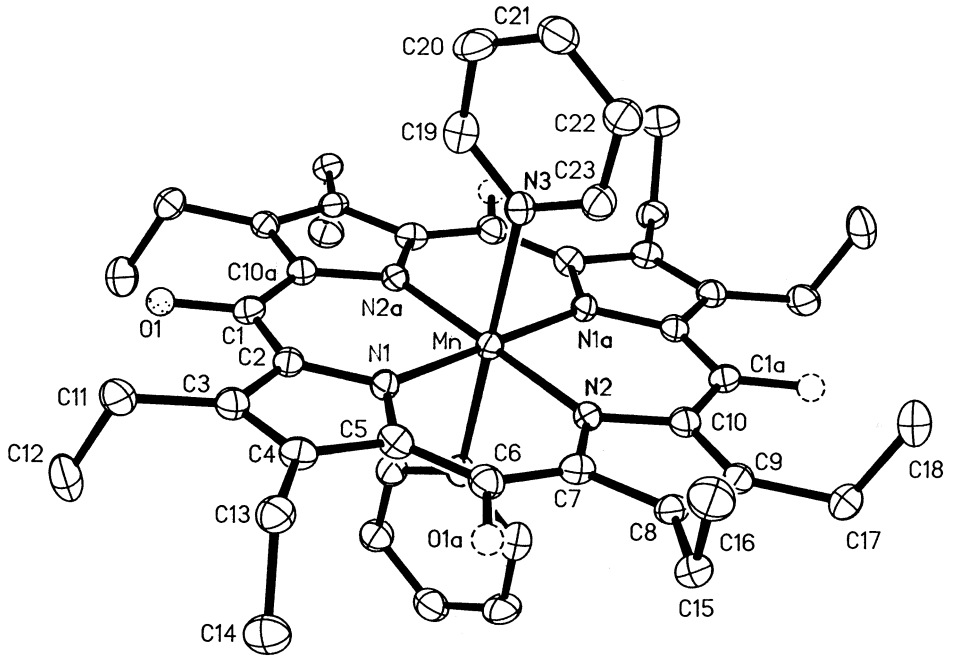

Fig. 4. The crystallographically determined structure of $\{(py)_2Mn^{III}(OEPO)\}$ (with 50% thermal contours), which shows the planarity of the macrocyclic core. Taken from Balch et al. [23].

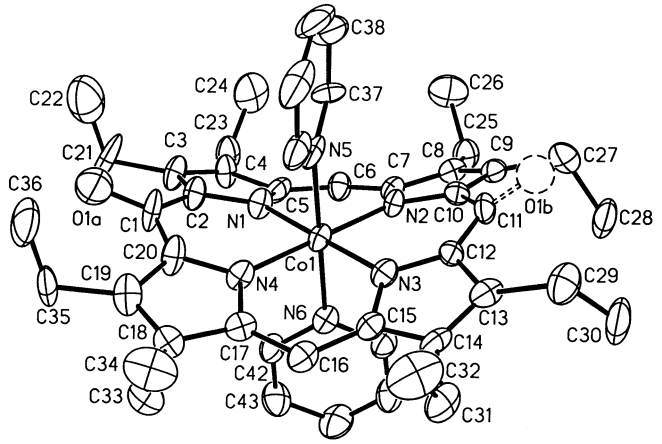

Fig. 5. A view of the crystallographically determined structure of $\{(py)_2Co^{III}(OEPO)\}$ with 50% thermal contours. Note the non-planarity of the macrocycle which contrasts with that of shown in Fig. 4. Taken from Balch et al. [17].

atom is disordered with 0.36 partial occupancy at sites O(1) and O(1b) and 0.14 occupancy for sites O(1a) and O(1aa). Treatment of $\{Fe^{III}(OEPO)\}_2$ with pyridine results in an analogous cleavage as described in Section 7 [22].

Treatment of $\{(py)Co^{II}(OEPOH\cdots py)\}$ with an oxidant, dioxygen or diiodine, in pyridine solution results in the formation of a lime–green solution which produces blue crystals of diamagnetic $\{(py)_2Co^{III}(OEPO)\}$ [17]. The crystallographically determined structure of the product is shown in Fig. 5. The relatively short Co–N distances, which fall in the range 1.948(7)–1.969(7) Å are characteristic of the presence of Co(III) and cause the ligand to undergo distort significantly from planarity as seen in Fig. 5. Again the *meso* oxygen atom is disordered with a site occupancy of 0.69(1) at the major site and 0.31(1) at the minor position.

6. Coordinated radicals

As noted in Section 1, free radical forms of the tetrapyrrole, **1**, have been known for some time [5–7], but only recently have metal complexes of these radicals been fully characterized. Complexes of the $\{M^{II}(OEPOH)\}$ type undergo unusually facile oxidation which can lead to either the formation of a ligand-based radical or to a change in the oxidation state of the metal. The course of the reaction is dependent on the metal within the complex and may be dependent on the coordination environment of the complex and the availability of axial ligands. Exposure of a red pyridine solution of $\{(py)Zn^{II}(OEPOH\cdots py)\}$ to air results in the gradual formation of a green solution from which crystals of

{(py)Zn^{II}(OEPO$^{\bullet}$)}·(py) are obtained [16]. The structure of {(py)Zn^{II}(OEPO$^{\bullet}$)}·(py) as determined by X-ray crystallography is shown in Fig. 6. Although there are two pyridine molecules in the compound, only one of these is coordinated to the zinc ion. The UV–vis absorption spectrum of {(py)Zn^{II}(OEPO$^{\bullet}$)} shows a broadened Soret band at 438 nm and a characteristic, low energy feature at 819 nm. The product has a magnetic moment of 1.8 μB in pyridine solution and exhibits an EPR resonance at $g = 2.0$ [16]. Fig. 7 shows the composition of the π-molecular orbital of the macrocycle that contains the unpaired electron [26,27]. The orbital coefficients reveal that the spin density within the radical is highest at the oxygen atom with significant spin density at the *meso* carbons, especially at the *meso* carbon *trans* to the oxygen atom. Interestingly oxidation terminates at this free radical stage, and the product is itself stable to air [16]. Another report on the structure of a zinc complex of H_2OEPOH has appeared, but the authors were unable to determine the protonation or oxidation state of the ligand in this complex [28].

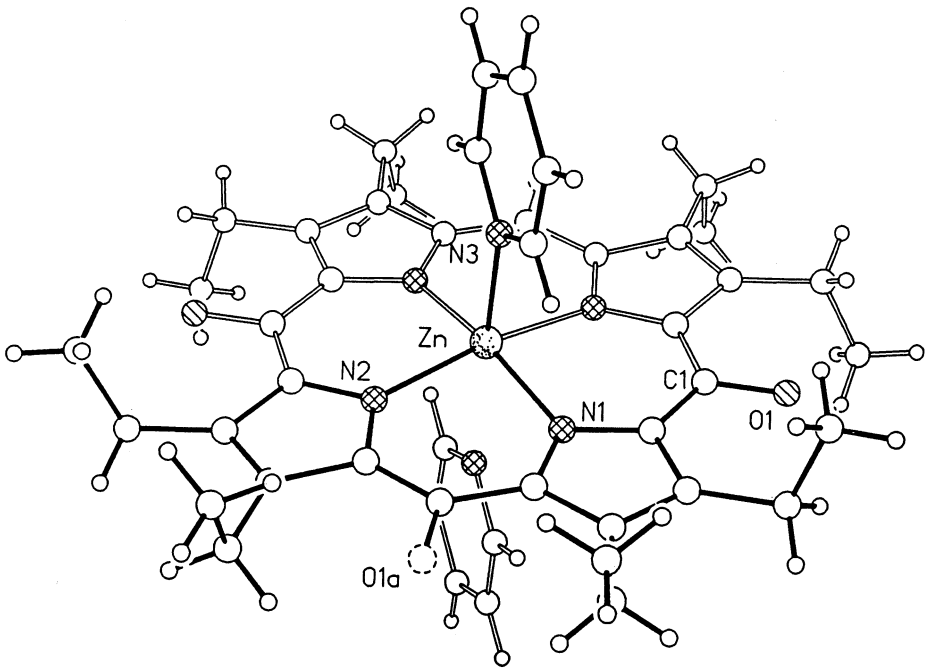

Fig. 6. The crystallographically determined structure of {(py)Zn^{II}(OEPO$^{\bullet}$)}. One pyridine molecule is coordinated to the zinc ion while the other is not. The complex resides at a center of symmetry. In half of the molecules, the zinc atom resides on one side of the porphyrin and is coordinated to the pyridine on that side, while in the other half of the molecules the zinc atom resides on the opposite side of the ligand plane and is coordinated to the other pyridine molecule. Additionally the *meso* oxygen atom is disordered with 29% site occupancy adjacent to C(1) and 21% occupancy adjacent to C(6). Taken from Balch et al. [16].

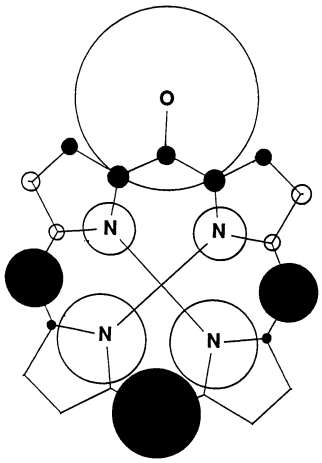

Fig. 7. A drawing of the magnitudes and phases of the π-molecular orbital that contains the unpaired electron in the ligand radical $(OEPO^{\bullet})^{2-}$. Taken from Balch et al. [27].

Aerial oxidation of Ni^{II}(OEPOH) in pyridine solution has been found to lead to some more complicated chemistry which is summarized in Scheme 5 [18,29].

Initially, oxidation forms the free radical complex, $\{(py)_2Ni^{II}(OEPO^{\bullet})\}$, which has been isolated in crystalline form. The axial ligands appear to stabilize this free radical complex through steric protection. When pyridine is removed, $\{Ni^{II}_2(OEPO)_2\}$ undergoes coupling and dimeric $\{Ni^{II}_2(OEPO)_2\}$ is produced. The structure of $\{Ni^{II}_2(OEPO)_2\}$ is shown in Fig. 8. The two macrocycles are joined through two *meso* carbon atoms. The crucial new C12–C48 bond has a length of 1.614(8) Å, which is at the long end of the range known for C–C single bonds. Note that the site of C–C bond formation corresponds to the major site of carbon atom unpaired spin density that is present in the π-molecular orbital which contains the unpaired electron in the parent radical (see Fig. 7). The two macrocycles have a pronounced saddle shape which complements each other in the areas where there is significant overlap.

As seen in Scheme 5, $\{(py)_2Ni^{II}(OEPO^{\bullet})\}$ is sensitive to further oxidation by dioxygen. This process results in further oxidation at the other two *meso* sites and in the formation of a mixture of *cis*-$\{(py)_2Ni^{II}(OEPO_2)\}$ and *trans*-$\{(py)_2Ni^{II}(OEPO_2)\}$ [18]. These two six-coordinate complexes have been independently prepared by insertion of Ni(II) into the corresponding dioxoporphyrin, H_2OEPO_2 and characterized by X-ray crystallography [30]. Notice that the further oxidation of $\{(py)_2Ni^{II}(OEPO^{\bullet})\}$ occurs at the sites of high carbon-atom spin density (see Fig. 7) within the parent radical complex.

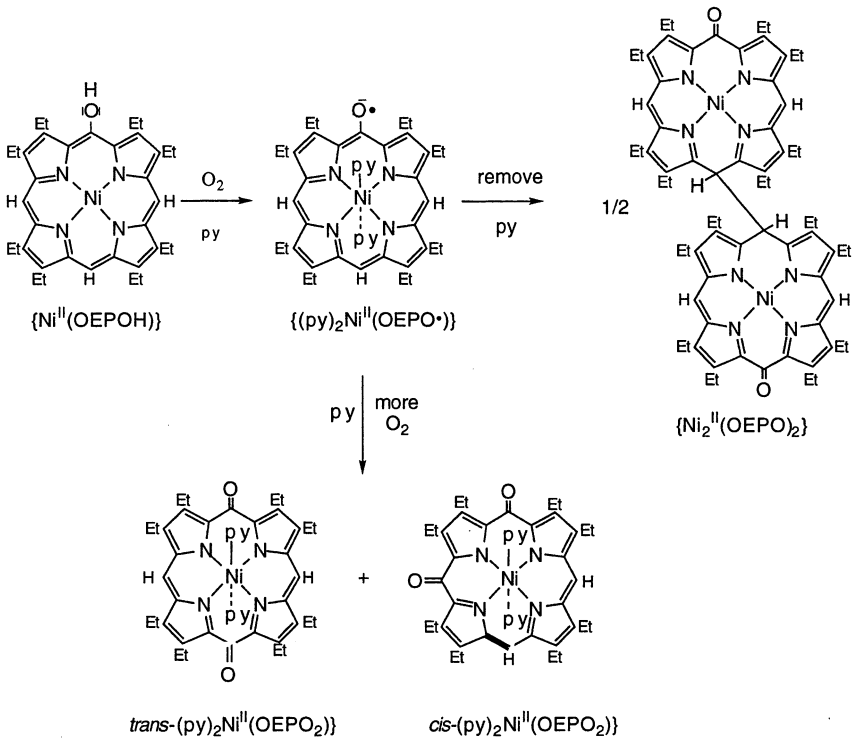

Scheme 5. Reactivity of nickel complexes.

Not all oxidations of complexes of the type $\{M^{II}(OEPOH)\}$ lead to the formation of relatively stable ligand radicals. As described above, treatment of $\{(py)Co^{II}(OEPOH\cdots py)\}$ with either dioxygen or diiodine produces $\{(py)_2Co^{III}(OEPO)\}$ in which the metal ion, not the ligand, has been oxidized [17].

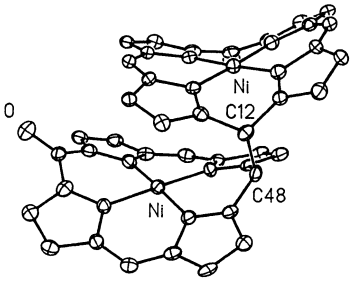

Fig. 8. A perspective view of the crystallographically determined structure of $\{Ni_2^{II}(OEPO)_2\}$ with 50% thermal contours. The two macrocyclic ligands are connected by a C–C bond between the *meso* carbon atoms C12 and C48. The ethyl groups are omitted for clarity. Data taken from Balch et al. [29].

7. Iron complexes

7.1. Model compounds

The coordination chemistry of iron complexes of *meso*-hydroxylated hemes has received significant attention due to the formation of such complexes during heme degradation. Scheme 6 summarizes the status of the chemistry that has been observed in model compounds with compounds obtained ultimately from octaethylporphyrin. Progress in characterizing these complexes has relied upon compound

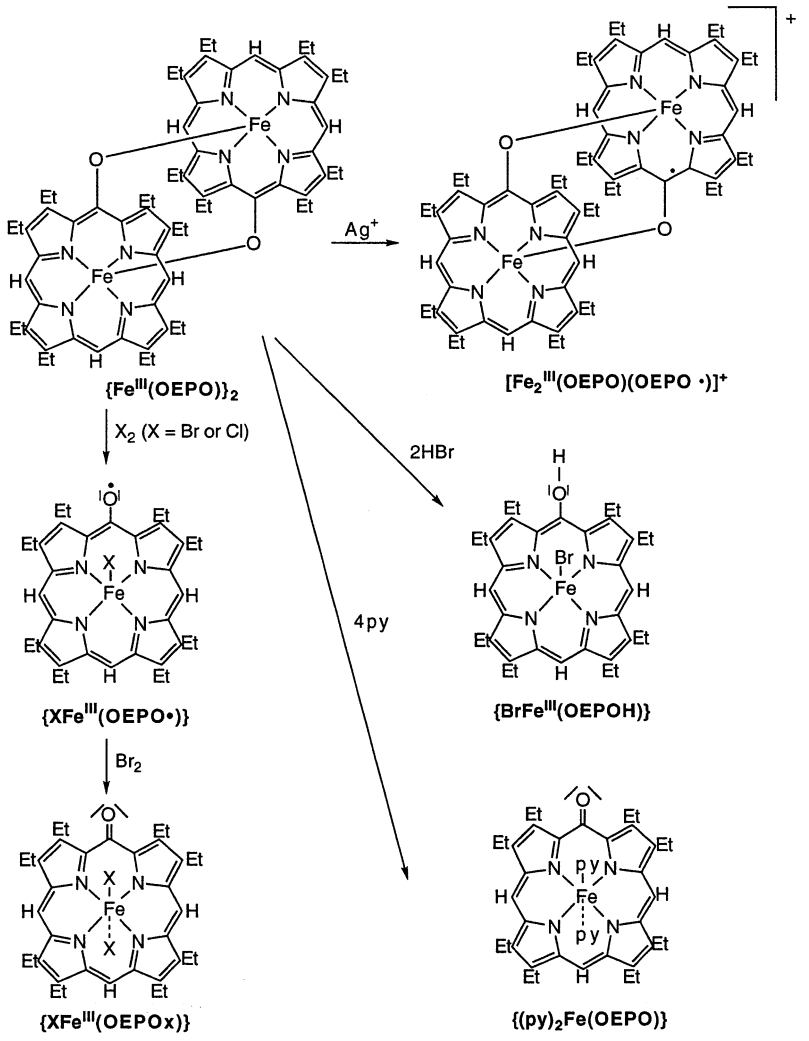

Scheme 6. Reactivity of iron complexes.

isolation, crystallography and spectroscopy. Table 1 gives relevant UV–vis spectral data for complexes that have been isolated and thoroughly characterized. ^{1}H NMR spectroscopy has been particularly important for the development in this area. Since most of the spin, oxidation, and ligation states of iron are paramagnetic, the ^{1}H NMR spectra that are observed show highly temperature dependent hyperfine shifts with dispersion over hundreds of ppm [31,32]. Table 2 gives a compilation of the chemical shifts observed for a representative set of these complexes.

The chemistry summarized in Scheme 6 starts with the dimer, $\{Fe^{III}(OEPO)\}_2$, which is the iron complex produced by direct metal ion insertion into the free ligand, H_2OEPOH [21,22]. However, this dimer is more conveniently obtained by coupled oxidation of $ClFe^{III}$(OEP) with dioxygen in the presence of an excess of potassium cyanide [33].

The spectroscopic properties of this dimer have been carefully studied [21,22]. The ^{1}H NMR spectrum of $\{Fe^{III}(OEPO)\}_2$ is shown in Fig. 9 [22]. The spectral pattern is typical of that expected for a high-spin ($S = 5/2$), five-coordinate iron(III) complex with very small antiferromagnetic coupling between the two iron centers. However, spectroscopic features that are influenced by paramagnetic relaxation, the line widths and T_1 values for the methylene resonances, show a noticeable variation which is caused by the presence of two paramagnetic centers in the dimer (see trace b of Fig. 9). Thus the two broadest methylene resonances (a and a′) arise from protons that are closest to the iron in the adjacent macrocycle and which undergo additional relaxation from that paramagnetic center.

The dimeric structure of $\{Fe^{III}(OEPO)\}_2$ remains intact as it undergoes reversible one-electron oxidation with Ag^+ to form $[\{Fe^{III}(OEPO)\}_2]^+$ [34]. The ^{1}H NMR spectra taken during an oxidative titration reveal that the two dimers are in fast electron exchange on the NMR time scale in solution and that the product has an electronic structure in which an electron has been removed from the ligands. Nevertheless, the unpaired electron in the dimeric cation is delocalized over both ligands, since only a single set of two *meso* C–H resonances and one set of eight resonances for the methylene groups are observed.

The dimer, $\{Fe^{III}(OEPO)\}_2$, also undergoes oxidation with molecular halogens, but these reactions result in rupture of the axial Fe–O bonds [27]. Addition of one equivalent of halogen (Cl_2 or Br_2) to the dimer produces five-coordinate

Table 1
UV–vis data for iron octaethyloxophlorin complexes

Compound	λ_{max} (nm)	Ref.
$ClFe^{III}$(OEPOAc)	388[a], 506, 642	[22]
$\{Fe^{III}(OEPO)\}_2$	390[a], 490, 530, 670, 1050	[21,22]
$\{Fe^{III}(OEPO)\}_2^+$	396[a], 560, 678	[34]
$BrFe^{III}(OEPO^{\bullet})$	406[a], 514, 683	[27]
Br_2Fe^{III}(OEPOx)	393[a], 449, 574	[27]
$(py)_2$Fe(OEPO)	425[a], 606, 649	[23,26,36,40]

[a] Soret band.

Table 2
^{1}H NMR data for iron octaethyloxophlorin complexes

Compound	Temperature, solvent	Chemical shifts (ppm)			Ref.
		Meso	Methylene	Methyl	
$ClFe^{III}$(OEP)	25°C, CD_2Cl_2	−56.0	44.5, 40.9	6.7	[22]
$BrFe^{III}$(OEPOH)[a]	25°C, $CDCl_3$	−71.7, −66.3	53.4, 49.6, 46.2, 44.3, 43.6,	8.7, 7.4, 7.1, 1.5	[22]
$\{Fe^{III}(OEPO)\}_2$	28°C, CD_2Cl_2	−98.4, −28.0	39.1, 37.1, 33.6, 31.8, 30.0, 28.8, 23.2, 18.0	5.2, 4.4, 4.1, −1.4	[22]
$\{Fe^{III}(OEPO)\}_2^+$	$CDCl_3$, DC_3CN	251, 243	105, 60, 50, 45, 38, 27, 24, 20		[34]
$BrFe^{III}(OEPO^{\bullet})$ **2**	25°C, $CDCl_3$	344.2, 232.2	65.5, 61.5, 59.3, 58.5, 2.30, −3.0, −15.1, −21.0	4.80[a], 4.60, 2.10	[27]
$ClFe^{III}(OEPO^{\bullet})$	25°C, $CDCl_3$	345.0, 232.7	61.8, 60.9, 58.2, 56.5, −2.2, −4.4, −17.0, −23.9		[27]
Br_2Fe^{III}(OEPOx) **3**	24°C, $CDCl_3$	35.4, 21.8	56.9, 49.9, 44.8, 33.4	6.97, 6.79, 6.14, 6.03	[27]
Cl_2Fe^{III}(OEPOx)	25°C, $CDCl_3$	23.9, 12.2	48.4, 42.6, 38.3, 20.0		[27]
$(py)_2$Fe(OEPO)	23°C, py	−153.9, 111.1	2.5, 2.1, 4.5, 31.6	3.5, 3.0, 2.8, 2.5	[23,26,36,40]

[a] Intensity double that of other methyl resonances.

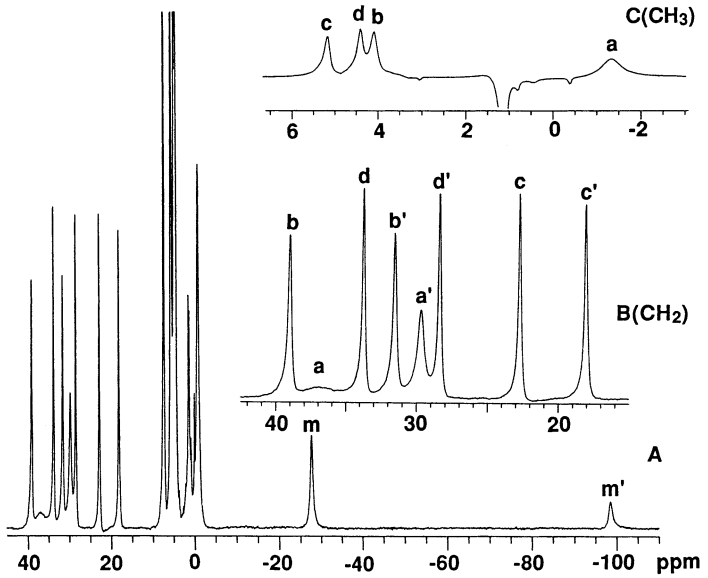

Fig. 9. The 300 MHz ^{1}H NMR spectrum of $\{Fe^{III}(OEPO)\}_2$ in chloroform-*d* solution at 28°C with the *meso* resonances designated by m and m′. Insert B shows an expansion of the region of methylene resonances while insert C shows the region of methyl resonances with selective inversion of resonances from the diamagnetic material in the sample. Data taken from Balch et al. [22].

$\{XFe^{III}(OEPO^{\bullet})\}$ whose crystallographically determined structure is shown in Fig. 10. The ^{1}H NMR spectrum of $\{BrFe^{III}(OEPO^{\bullet})\}$ is shown in Fig. 11. The spectrum reveals a pattern of hyperfine shifts (with the *meso* resonances far downfield and

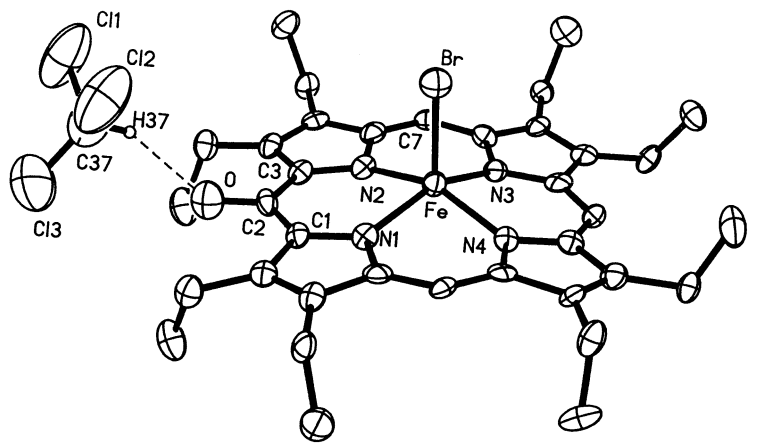

Fig. 10. A view of the crystallographically determined structure of $\{BrFe^{III}(OEPO^{\bullet})\}\cdot CHCl_3$ with 50% thermal contours. Note that the chloroform molecule is hydrogen bonded to the *meso* oxygen atom of the macrocycle. Taken from Balch et al. [27].

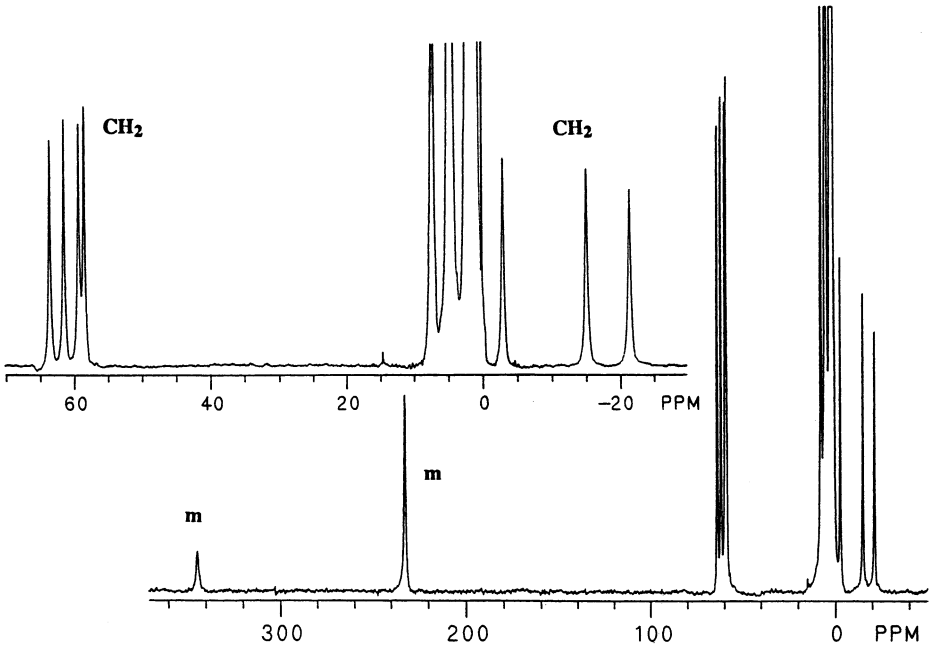

Fig. 11. The ^{1}H NMR spectrum of {BrFe^{III}(OEPO$^{\bullet}$)} in chloroform-*d* solution at 24°C. Insert A shows an expanded section of the methylene resonances near 60 ppm, while B shows the methyl and methylene resonances in the 6 to −4 ppm region under inversion recovery conditions that invert resonances of diamagnetic compounds. Taken from Balch et al. [27].

with four methylene resonances shifted upfield and the four other methylene resonances shifted downfield) that is consistent with a ligand-based oxidation. The occurrence of eight methylene resonances is indicative of the five-coordinate structure which renders the two sides of the porphyrin plane inequivalent and each methylene group diastereotopic. The magnetic moment, 4.9 μB at 298 K, has been interpreted in terms of a high-spin ($S = 5/2$) Fe(III) center which is antiferromagnetically coupled to an $S = 1/2$ site on the ligand.

Further oxidation of {Fe^{III}(OEPO)}$_2$ or {XFe^{III}(OEPO$^{\bullet}$)} with dichlorine or dibromine results in the formation of {X$_2$Fe^{III}(OEPOx)} [27]. The six-coordinate product has properties that indicate the presence of high-spin Fe(III) and a fully oxidized ligand. The magnetic moment of the complex is 5.8 μB, which is close to the spin only value expected for such an iron(III) complex. The complex, {Br$_2$Fe^{III}(OEPOx)}, displays a paramagnetically shifted ^{1}H NMR spectrum which is shown in Fig. 12. This spectrum corresponds to the spectra that have been seen for six-coordinated Fe(III) complexes of porphyrins [35]. The complex displays an EPR spectrum that is also typical of high-spin Fe(III) with $g = 5.9$ and 2.0 and with super hyperfine splitting on the $g = 2.0$ line due to coupling to two equivalent bromide ligands [27].

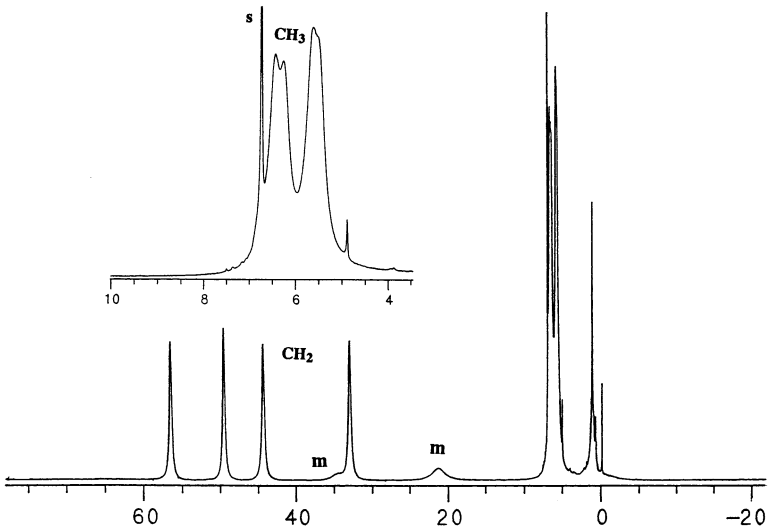

Fig. 12. The 300 MHz ^{1}H NMR spectrum of {Br_2Fe^{III}(OEPOx)} in chloroform-*d* solution at 24°C. Insert A shows an expanded section of the methyl resonances in the 10–4 ppm region. Taken from Balch et al. [27].

Dimeric {Fe^{III}(OEPO)}$_2$ also undergoes the two reactions, cleavage by acid (HCl or HBr) and cleavage by base (pyridine) as previously described for such dimers in Scheme 4 [21–23]. Of these, cleavage by pyridine is particularly important for that reaction produces, {(py)$_2$Fe(OEPO)}, which is a widely used model for the hydroxylated heme formed during the process of heme degradation by heme oxygenase. Solutions of {(py)$_2$Fe(OEPO)} can also be obtained by anaerobic hydrolysis of the (*meso*-benzyloxy)octaethylheme, {ClFe^{III}(OEPOC(O)Bz)}, in pyridine solution [26,36]. Solutions of {(py)$_2$Fe(OEPO)} are air sensitive, nevertheless the complex has been subject to extensive study, initially by Morishima and coworkers. The complex shows a UV–vis absorption spectrum with a broadened Soret band at 425 nm and a distinctive feature at 649 with a shoulder at 606 nm [26,36]. It is EPR silent at room temperature but shows an axial spectrum with $g = 2.31$ and 1.75 at 77 K. It has a magnetic moment of 2.4 μB at 23°C in pyridine solution [26,36]. The ^{1}H NMR spectrum, which is shown in Fig. 13, is unlike that of any other Fe(II) or Fe(III) porphyrin complex but is particularly useful in monitoring the reactivity of this species [26,36]. (An earlier report of the ^{1}H NMR spectrum of this compound appears now to have resulted from a mixture of heme oxidation products [37].) Addition of acids to pyridine solutions of {(py)$_2$Fe(OEPO)} produce marked changes in the ^{1}H NMR spectrum with all resonances experiencing smaller paramagnetic shifts as seen in Fig. 13 [26,36]. These changes have been interpreted as resulting from protonation of the oxygen atom in the complex. The electronic structure of this unusual complex, {(py)$_2$Fe(OEPO)}, has been described in terms of three possible distributions of electrons between the metal and ligand as shown in Scheme 7 [22,26,39]. The spectroscopic properties of have been interpreted in favor

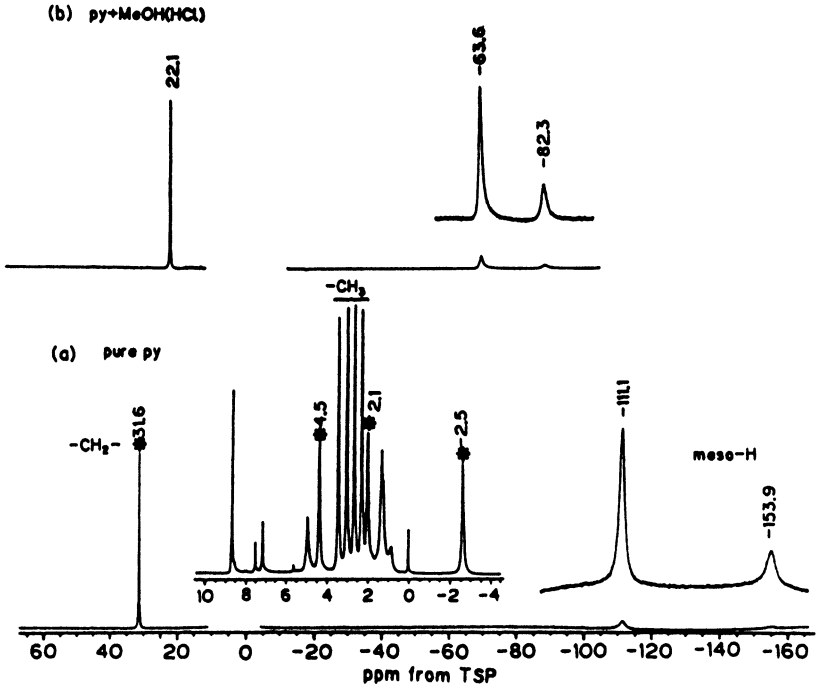

Fig. 13. The ^{1}H NMR spectrum of {(py)$_2$Fe(OEPO)} in pyridine-d_5 solution (bottom) and with methanolic hydrogen chloride added (top) at 23°C. Taken from Morishima et al. [26].

of a principle contribution coming from an $Fe^{II}/(OEPO^{\bullet})^{2-}$ electronic distribution with the iron in a low-spin ($S = 0$) state [26,36]. The unusual pattern of resonances in the ^{1}H NMR spectrum of {(py)$_2$Fe(OEPO)} suggests that there is a significant contribution from a ligand-based radical. The non-Curie behavior observed in the variable temperature ^{1}H NMR spectrum suggests that there are temperature dependent changes occurring in the electronic distribution within the complex. The

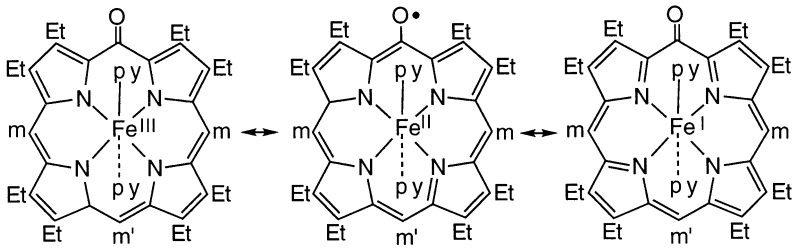

Scheme 7. Electronic distributions within {(py)$_2$Fe(OEPO)}.

^{1}H NMR spectrum of this complex has also been interpreted in terms of a low-spin $(d_{xz}d_{yz})^4(d_{xy})^1$ ground state [28]. However, this interpretation is at odds with the results of the crystallographic study of the isolated complex (vide infra). Additional complexes related to {$(py)_2$Fe(OEPO)} but with different axial ligands, imidazoles [36], isocyanides [21], and cyanide ion [33], have also been detected and show ^{1}H NMR spectra similar to those seen in Fig. 13.

Additionally, the corresponding complex of protoheme (see Scheme 2) with hydroxylation exclusively at the α-*meso* site has been prepared and characterized spectroscopically by Sano and coworkers [39]. This complex is prepared by anaerobic hydrolysis of α-(*meso*-benzyloxy)protoheme in pyridine solution and has been used to incorporate this intermediate into proteins.

By skilful manipulation, it has been possible to isolate {$(py)_2$Fe(OEPO)} in crystalline form [40]. Fig. 14 shows a drawing of the molecule. The oxygen atom is not protonated, and the C–O bond length, 1.289(4) Å, is consistent with the presence of keto group. The most remarkable features of the structure are the Fe–N bond lengths, Fe–N(10), 2.055(2), Fe–N(2), 2.051(2) and Fe–N(3), 2.265(2)

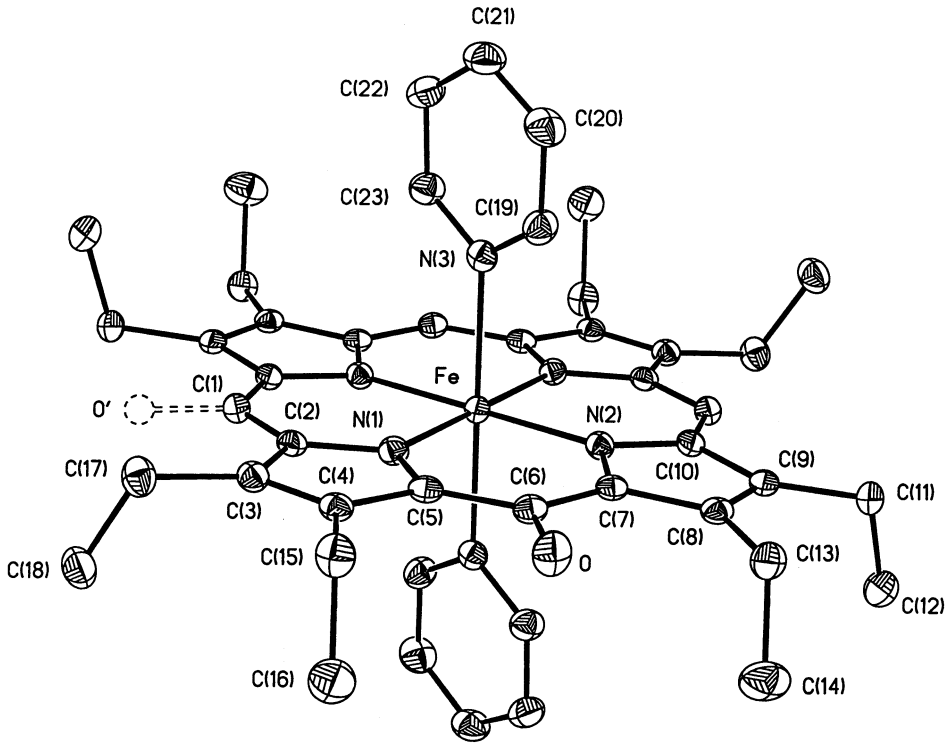

Fig. 14. A drawing of the crystallographically determined structure of {$(py)_2$Fe(OEPO)} with 50% thermal contours. The iron atom is situated at a crystallographic inversion center and the oxygen atom is disordered. At site O, the oxygen atom occupancy is 0.39, while it is 0.11 at site O′. Taken from Balch et al. [40].

Å, which indicate that the iron is in a high-spin state in the crystalline solid. Thus, the solid state structure is inconsistent with the interpretation of the ^{1}H NMR spectrum in terms of a low-spin $(d_{xz}d_{yz})^4(d_{xy})^1$ ground state which is generally stabilized by a distorted heme plane and a perpendicular arrangement of the axial pyridine ligands [38]. Note that in the structure shown in Fig. 14, the heme is planar and the pyridine ligands are parallel to one another. However, the electronic structure of this complex in the solid state may differ from that present in solution, and further work in defining the electronic distribution within this unusual complex and related complexes with different axial ligands is warranted. For example it is difficult to believe that the cyano complex, $[(NC_2Fe(OEPO)]^{2-}$, which has an ^{1}H NMR spectrum analogous to that of $\{(py)_2Fe(OEPO)\}$ [33], is high-spin.

Electrochemical studies reveal that $\{(py)_2Fe(OEPO)\}$ undergoes two reversible, one-electron transfer processes as outlined in Scheme 8 [40]. Spectroscopic properties (UV–vis, 424, 608, 648 nm, ^{1}H NMR spectrum) have been obtained for the oxidized species, $[(py)_2Fe(OEPO)]^+$ but not for the reduced form of the complex. The ^{1}H NMR spectrum of $[(py)_2Fe(OEPO)]^+$ consists of *meso* and methylene resonances that are found in the narrow 5–2 ppm range (at -20°C), and the temperature dependence of the spectrum suggest that this even-electron complex has a diamagnetic ground state with paramagnetic state that is partially populated [40]. The chemical reactivity of $[(py)_2Fe(OEPO)]^+$ and its role in heme destruction remain to be determined.

By studying the oxidation of the simple, low-spin heme, $(py)_2Fe^{II}(OEP)$, by dioxygen in the presence of hydrazine (as sacrificial reducing agent) at low temperature (ca. -30°C), it has been possible to show through ^{1}H NMR studies that $\{(py)_2Fe(OEPO)\}$ and the related complexes, $\{(py)(N_2H_4)Fe(OEPO)\}$ and $\{(N_2H_4)_2Fe(OEPO)\}$, are intermediates in the coupled oxidation of iron(II) porphyrins [41]. Relevant data are shown in Fig. 15. This coupled oxidation process, which has been widely used as a model for biological heme degradation, yields the verdoheme, $[(py)_2Fe^{II}(OEOP)]Cl$ [42,43], and the iron complex of octaethylbilindione, $\{(py)_2Fe^{III}(OEB)\}$ [44], as seen in Scheme 9. Solutions of $\{(py)_2Fe(OEPO)\}$ in pyridine are very air sensitive. Exposure of pyridine solutions of $\{(py)_2Fe(OEPO)\}$ to dioxygen results in the direct formation of $[(py)_2Fe^{II}(OEOP)]Cl$ and $\{(py)_2Fe^{III}(OEB)\}$ without the need for the addition of a reducing agent. As shown in Scheme 9, there are two stages to the coupled oxidation process. In the first part the porphyrin undergoes what amounts to hydroxylation of one of the *meso* carbon atoms with the formation of $\{(py)_2Fe(OEPO)\}$, $\{(py)(N_2H_4)Fe(OEPO)\}$, and $\{(N_2H_4)_2Fe(OEPO)\}$, which are in equilibrium with one another in the presence of hydrazine and pyridine. In the presence of dioxygen, which destroys hydrazine through oxidation, these three intermediates are converted into just

$$(py)_2Fe^{II}(OEPOH)\} \underset{+e^-,\,+H^+}{\overset{-e^-,\,-H^+}{\rightleftharpoons}} \{(py)_2Fe(OEPO)\} \underset{+e^-}{\overset{-e^-}{\rightleftharpoons}} [(py)_2Fe(OEPO)]^+$$

Scheme 8. Redox reactions of $\{(py)_2Fe(OEPO)\}$.

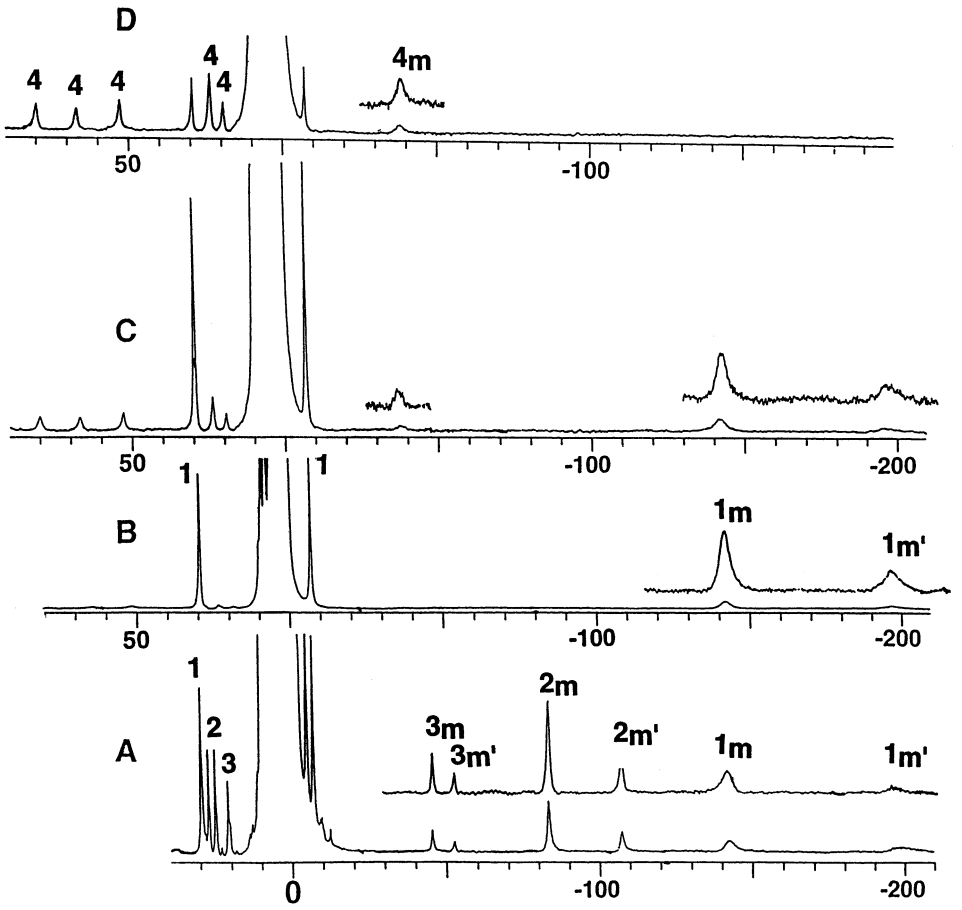

Fig. 15. 300 MHz ^{1}H NMR spectra from the reaction of {(py)$_2$Fe^{II}(OEP)} in dichloromethane-d_2/pyridine-d_5 (6.7/1, v/v) with hydrazine-d_4 at −30°C. Trace A, immediately after the addition of dioxygen. Trace B, after 10 min at −30°C. Trace C, after the NMR tube is shaken for 30 s and placed back in the −30°C probe. Trace D, after an additional 20 min has elapsed. Resonances of individual complexes are labeled: 1, {(py)$_2$Fe(OEPO)}; 2, {(py)(N$_2$D$_4$)Fe(OEPO)}; 3, {(N$_2$D$_4$)$_2$Fe(OEPO)}; and 4, {(py)$_2$Fe^{III}(OEB)}. Subscripts m and m′ refer to *meso* C–H resonances. Taken from St. Claire and Balch [41].

{(py)$_2$Fe(OEPO)}. In the second stage, {(py)$_2$Fe(OEPO)} reacts with dioxygen to yield [(py)$_2$Fe^{II}(OEOP]Cl and {(py)$_2$Fe^{III}(OEB)}. This stage is undoubtedly a multistep process that results in the eventual rupture of two C–C bonds and liberation of carbon monoxide.

7.2. Detection in proteins

Evidence for the involvement of *meso*-hydroxylated hemes, **1**, during heme catabolism has come from experiments in which the *meso*-hydroxylated heme is

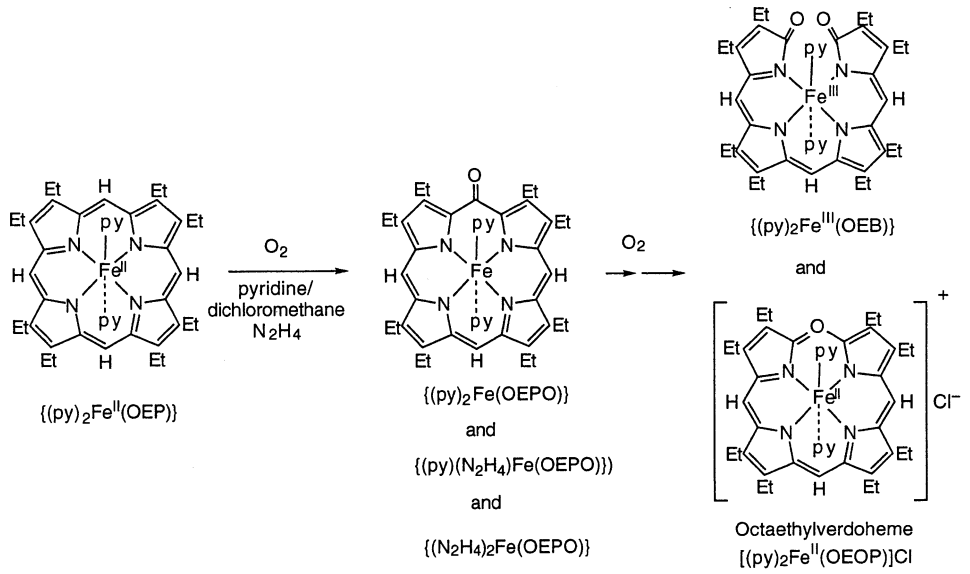

Scheme 9. Coupled oxidation of heme.

incorporated into a protein or in which it has been trapped as an intermediate during heme oxidation. Studies have been conducted with both heme oxygenase and with myoglobin, which acts as a model protein that provides a structurally well-defined heme binding pocket. Additionally, the heme in myoglobin undergoes regiospecific cleavage at the α-*meso* site to form biliverdin and carbon monoxide when the protein is treated under coupled oxidation conditions with dioxygen in the presence of a reductant (ascorbic acid or hydrazine) [45]. Thus, in this stoichiometric reaction myoglobin mimics the action of heme oxygenase.

The initial evidence for the existence of heme **1** as an intermediate in heme catabolism came from experiments in which the hydroxylated heme was found to serve as a substrate for heme oxygenase and produce biliverdin as the product [46]. Subsequently, the four isomeric *meso*-oxyprotohemes were prepared from the corresponding (*meso*-benzyloxy)protoheme isomers after separation [39]. These individual isomers were then used as substrates for heme oxygenase [47]. Only the α-isomer was converted to biliverdin IXa, which could be further reduced to bilirubin [47]. The ability of heme oxygenase to use the iron complex of **1** as a substrate with the observed specificity presented compelling evidence that the initial stage of heme catabolism involves hydroxylation of one specific *meso* site by an dioxygen derived species

Treatment of heme in heme oxygenase with hydrogen peroxide produces verdoheme, and with ethyl hydroperoxide the reaction proceeds regiospecifically to produce α-(*meso*-ethoxy)protohemin [48]. This reaction has been interpreted by Ortiz de Montellano and co-workers to indicate that the initial stage of the heme oxygenase reaction proceeds by electrophilic or radical addition of the distal oxygen of an iron-bound peroxide to the α-*meso* site of the porphyrin.

Anaerobic addition of α-(hydroxy)protoheme to heme oxygenase and to apomyoglobin has allowed the direct spectral observation of this modified heme within the respective protein cavities [49]. This has lead to the characterization of a ferric, α-oxygenated form of heme oxygenase with a UV–vis spectrum with λ_{max} of 406 nm (and a featureless visible region) with a rhombic EPR spectrum that shows $g = 6.08$, 5.73, and 2.004. These spectra have been analyzed in favor of the existence of a five-coordinate, high-spin Fe(III) center in this protein-bound intermediate. Suitable models for such a five-coordinate high-spin Fe(III) complex of the *meso*-hydroxylated heme **1** are currently unavailable. Resonance Raman spectra have also been observed for the ferric, α-oxygenated form of heme oxygenase that are quite different from typical heme protein Raman spectra. Since these resonance Raman spectra do not change upon going from H_2O to D_2O, it appears that the *meso* oxygen atom does not bear a proton in this redox state. Dithionite reduction of this intermediate form results in spectral changes (UV–vis, Soret band at 432 nm, Raman spectra characteristic of heme complexes) that are indicative of the formation of a heme-like penta-coordinate, high-spin Fe(II) species. The resonance Raman spectra show H_2O/D_2O changes that are consistent with protonation of the *meso* oxygen atom upon reduction. This state of the protein undergoes conversion to verdoheme when treated with dioxygen and addition of carbon monoxide to produce a UV–vis spectrum with a broadened Soret band at 410 nm.

Similar UV–vis and resonance Raman spectral data have been obtained by treating protoheme in heme oxygenase with hydrogen peroxide under anaerobic conditions [50]. This set of experiments provides direct evidence that the α-(*meso*-hydroxy)protoheme is formed during functioning of heme oxygenase. However, this experiment also produces an EPR resonance at $g = 2.008$ that is not observed when heme oxygenase binds α-(hydroxy)protoheme. The resonance has been attributed to a 'ferrous π neutral radical species' [50]. The intensity of this feature in the spectrum is enhanced by the addition of carbon monoxide, but the resonance itself is unchanged. Further characterization of the species responsible for this EPR signal appears warranted.

A bacterial heme oxygenase has been found to operate in a similar manner to that of mammalian heme oxygenase [51].

The conversion of α-(*meso*-hydroxy)protoheme to verdoheme in heme oxygenase is a chemically complex process that involves cleavage of two carbon–carbon bonds and release of carbon monoxide. Biochemically, the process has become the subject of controversy [49,50,52,53]. At issue are the questions of whether the five-coordinate, high-spin Fe(III) α-(*meso*-hydroxy)protoheme complex of heme oxygenase requires additional electrons before reacting with dioxygen to yield verdoheme and what is the redox state of the iron in the verdoheme that is produced. Ikeda-Saito and co-workers found that the ferric hydroxyheme in heme oxygenase required both dioxygen and one electron to form verdoheme. However, Ortiz de Montellano and coworkers reported that the Fe(III) α-(*meso*-hydroxy)protoheme complex of heme oxygenase reacts directly with dioxygen without the need for reducing equivalents to yield the Fe(III) redox state of verdoheme [50]. Noguchi and coworkers report that the Fe(III) α-(*meso*-hydroxy)protoheme complex of heme

oxygenase is converted to the verdoheme by reaction with dioxygen again without the need for additional reducing agent but that the verdoheme so produced is on the Fe(II) redox state [52]. Recently, Migita and coworkers have reported that five-coordinate, high-spin Fe(III) α-(*meso*-hydroxy)protoheme complex can undergo an oxidation with either dioxygen or [hexachloroiridium(IV)]$^{2-}$ to yield a more highly oxidized form with a modest shift in the Soret band from 405 to 401 nm [53]. Under these conditions oxidation to form verdoheme is unproductive. The behavior of this five-coordinate protein-bound system appears to be paralleling the behavior already seen in the six-coordinate model compounds shown in Scheme 8 with three redox-linked oxidation states of the heme complex. However, the details surrounding the sequence of redox transformations necessary to convert α-(*meso*-hydroxy)protoheme complex of heme oxygenase into verdoheme remain to be satisfactorily resolved.

Ikeda-Saito, Hoffman and co-workers have conducted a series of EPR studies on the low temperature (77 K) reduction of the diamagnetic, dioxygen complexes of heme oxygenase and of hemoglobin β-chains [54]. In both cases a low-spin Fe(III) heme is produced with $g = 2.37$, 2.19, and 1.93 (at 77 K) for the intermediate bound to heme oxygenase. Proton ENDOR spectra have detected the presence of a an exchangeable hydrogen in this intermediate. These spectral characteristics have been assigned to an end-on bound Fe(III) peroxo species which is hydrogen bonded. Upon warming this intermediate above 200 K, its EPR spectrum disappears and is replaced by a high-spin Fe(III) spectrum which has been identified as resulting from the formation of the high-spin Fe(III) α-(*meso*-hydroxy)protoheme complex of heme oxygenase. Thus, the hydroperoxy Fe(III) heme complex of heme oxygenase self-hydroxylates.

8. Conclusions

The results described here show that there is a rich coordination chemistry associated with the *meso*-hydroxylated porphyrins and that these complexes have a direct relevance to the process of heme catabolism. The modified heme **1** is unusually susceptible to oxidation, but several paths of oxidative reactivity have been observed. By studying the reactivity of this macrocycle toward a variety of different transition metals, it has been possible to sort out reactivity that is metal dependent from that which is intrinsically ligand based. Thus, oxidation of the zinc and nickel complexes, {(py)Zn^{II}(OEPOH$^{\cdot}$py)} and {Ni^{II}(OEPOH)}, produce relatively stable free radicals in which the odd electron is largely delocalized on the tetrapyrrole macrocycle. These stable odd-electron complexes show reactivity that is typical of radicals: coupling to yield a carbon–carbon bonded dimer as seen in Scheme 5 and Fig. 8 and reactivity toward dioxygen to yield oxygenation at *meso* sites as seen again in Scheme 5. In these transformations, reactivity is directed, as expected, to the sites of highest spin density as seen in the molecular orbital shown in Fig. 7. Additionally it is important to point out the difference in dimerization found for complexes of **1** and the dimerization of related porphyrin radicals

observed by Scheidt and coworkers. While dimerization of the nickel complex, $\{(py)_2Ni^{II}(OEPO^{\bullet})\}$, yields $\{Ni^{II}_2(OEPO)_2\}$ with a definite C–C bond; self association of porphyrin radicals, e.g. $[Mg^{II}(OEP^{\bullet})]^+$ [55], $[M^{II}(OEP^{\bullet})]^+$ (M = Ni, Cu) [56], $[(H_2O)Zn^{II}(OEP^{\bullet})]^+$ [57], and $[ClFe^{III}(OEP^{\bullet})]^+$ [58], occurs in a face-to-face fashion to produce dimers, which lack any covalent link between the two components. Moreover, these radicals also associate with the corresponding neutral porphyrin complexes to form mixed-valence species, e. g. $[Pd^{II}(OEP^{\bullet}/2)]_2(ClO_4)$ [59]. This type of association has not been observed with metal complexes of **1**.

The iron complexes obtained from **1** show very different behavior. Although there is strong physical evidence from spectroscopic studies that coordinated free radical forms are significant contributors to the electronic structure of some of these iron complexes, the intrinsic reactivity of these complexes differs from that shown in Scheme 5 for more ligand-based free radicals. Thus, oxidation of $\{(py)_2Fe(OEPO)\}$ occurs at the carbon atoms immediately adjacent to the oxygenated *meso* carbon atom and produces verdoheme and iron biliverdin as seen in Scheme 9. In regard to the further oxidation and ring opening of iron complexes of **1**, it is also clear that the state of the *meso* oxygenated portion is crucial. When that oxygen is bonded to another group as it is in $\{Fe^{III}(OEPO)\}_2$, $\{ClFe^{III}(OEPOC(O)Bz)\}$, and $\{ClFe^{III}(OEPOH)\}$, the complexes are stable to oxidation by dioxygen. However, the deprotonated complex, $\{(py)_2Fe(OEPO)\}$, which is at the same overall oxidation level as the three complexes — $\{Fe^{III}(OEPO)\}_2$, $\{ClFe^{III}(OEPOC(O)Bz)\}$, and $\{ClFe^{III}(OEPOH)\}$ — is highly susceptible to oxidation and ring opening by dioxygen.

A number of issues regarding the formation and reactivity of the α-(*meso*-hydroxy)protoheme complex of heme oxygenase remain to be understood. Model compounds for the five-coordinate forms that are present in the protein environment are currently unavailable. This situation occurs because of the stability of the dimer, $\{Fe^{III}(OEPO)\}_2$, which can only be cleaved by adding an excess of an appropriate axial ligand such as pyridine or imidazole and six-coordinate complexes result.

The factors that result in the regioselectivity of the initial protoheme hydroxylation and the exclusive formation of the α-*meso* isomer remain to be fully explained. Specificity has been suggested to be a consequence of the ability of the heme binding site to orient the heme-bound dioxygen toward the α-*meso* site [60,61]. It is expected that as more information of the structure and structural dynamics of the heme binding site within heme oxygenase become available, this issue may be clarified [62–64]. Recently, the crystal structure of human heme oxygenase-1 with the substrate (heme) bound has been reported [65]. The heme is sandwiched in between two helical protein segments with the proximal helix providing histidine 25 as an axial ligand. There are two molecules of the heme/heme oxygenase complex in the asymmetric unit. One of these molecules offers more confinement of the heme with the distal helix restricting access to the β-, γ- and δ-*meso* carbon atoms while the other molecule provides less steric constraint with both the α- and δ-*meso* carbon atoms accessible to attack. There are no specific basic or acidic residues in proximity to the α-*meso* carbon to participate in the *meso*-hydroxylation step.

While the crystal structure does support the notion of steric control of the regiochemistry of the initial hydroxylation, electronic factors may also play a role in directing this step, especially with non-natural heme substrates.

The process of dioxygen activation that results in the conversion of the *meso*-hydroxylated hemes into verdoheme and biliverdin is also a complex, multi-step process that requires opening of two carbon–carbon bonds. The chemical processes involved have received almost no study, although the possibility that the process occurs stepwise with the production of a formylbiliverdin intermediate in which only one of the carbon–carbon bonds broken has been considered [66]. It has been shown that formylbiliverdin complexes can be oxidatively transformed into verdoheme-type complexes [66].

Acknowledgements

The author thanks the National Institutes of Health (Grant GM26226) for support and all the co-workers, who are listed in the references, and especially Professor Latos-Grażyński and Ms. H. Kalish for their contributions in preparing this manuscript.

References

[1] D. Dolphin ((Ed.), The Porphyrins, Academic Press, New York, 1978.
[2] P.S. Clezy, in: D. Dolphin (Ed.), The Porphyrins, vol. 2, Academic Press, New York, 1978, p. 103.
[3] A.H. Jackson, G.W. Kenner, K.M. Smith, J. Chem. Soc. (C) (1968) 302.
[4] R. Bonnett, M.J. Dimsdale, J. Chem. Soc. Perkin Trans. (1972) 2540.
[5] P.S. Clezy, F.D. Looney, A.W. Nichol, G.A. Smythe, Aust. J. Chem. 19 (1966) 1481.
[6] J.-H. Fuhrhop, S. Besecke, J. Subramanian, J. Chem. Soc. Chem. Commun. (1973) 1.
[7] J.-H. Fuhrhop, S. Besecke, J. Subramanian, C.hr. Mengersen, D. Riesner, J. Am. Chem. Soc. 97 (1975) 7141.
[8] M.D. Maines, Heme Oxygenase: Clinical Applications and Functions, CRC Press, Boca Raton, FL, 1992.
[9] P.R. Ortiz de Montellano, Accounts Chem. Res. 31 (1998) 543.
[10] A. Gossauer, Chimia 48 (1994) 352.
[11] D.M. Bissell, Bile pigments and jaundice, in: J.D. Ostrow (Ed.), Liver: Normal Function and Disease, vol. 4, Marcel Decker, New York, 1986, p. 133.
[12] R. Schmid, A.F. McDonagh, in: D. Dolphin (Ed.), The Porphyrins, vol. 6, Academic Press, New York, 1979, p. 258.
[13] S.B. Brown, in: K.P.M. Heirwegh, S.B. Brown (Eds.), Bilirubin, vol. 2, CRC Press, Boca Raton, FL, 1982, p. 1.
[14] P. O'Carra, in: K.M. Smith (Ed.), Porphyrins and Metalloporphyrins, Elsevier, New York, 1975, p. 122.
[15] G.H. Barnett, M.F. Hudson, S.W. McCombie, K.M. Smith, J. Chem. Soc. Perkin Trans. 1 (1973) 691.
[16] A.L. Balch, B.C. Noll, E.P. Zovinka, J. Am. Chem. Soc. 114 (1992) 3380.
[17] A.L. Balch, M. Mazzanti, M.M. Olmstead, Inorg. Chem. 32 (1993) 4737.
[18] A.L. Balch, B.C. Noll, S.L. Phillips, S.M. Reid, E.P. Zovinka, Inorg. Chem. 32 (1993) 4730.
[19] W.R. Scheidt, Y.J. Lee, Struct. Bond. (Berlin) 64 (1987) 1.

[20] A.L. Balch, B.C. Noll, M.M. Olmstead, S.M. Reid, J. Chem. Soc. Chem. Commun. (1993) 1088.
[21] N. Masuoka, H.A. Itano, Biochemistry 26 (1987) 3672.
[22] A.L. Balch, L. Latos-Grażyński, B.C. Noll, M.M. Olmstead, E.P. Zovinka, Inorg. Chem. 31 (1992) 2248.
[23] A.L. Balch, B.C. Noll, S.M. Reid, E.P. Zovinka, Inorg. Chem. 32 (1993) 2610.
[24] E. Zovinka, PhD Thesis, University of California, Davis, 1993.
[25] J. Wojaczyński, L. Latos-Grażyński, M.M. Olmstead, A.L. Balch, Inorg. Chem. 36 (1997) 4548.
[26] I. Morishima, H. Fujii, Y. Shiro, S. Sano, J. Am. Chem. Soc. 108 (1986) 3858.
[27] A.L. Balch, L. Latos-Grażyński, B.C. Noll, L. Szterenberg, E.P. Zovinka, J. Am. Chem. Soc. 115 (1993) 11846.
[28] M.O. Senge, K.M. Smith, J. Chem. Soc. Chem. Commun. (1992) 1108.
[29] A.L. Balch, B.C. Noll, S.M. Reid, E.P. Zovinka, J. Am. Chem. Soc. 115 (1993) 2531.
[30] A.L. Balch, M.M. Olmstead, S.L. Phillips, Inorg. Chem. 32 (1993) 3931.
[31] G.N. La Mar, F.A. Walker, in: D. Dolphin (Ed.), The Porphyrins, vol. 4, Academic Press, New York, 1978, p. 61.
[32] F.A. Walker, U. Simonis, NMR of paramagnetic molecules, in: L.J. Berliner, J. Reuben (Eds.), Biological Magnetic Resonance, vol. 12, Plenum Press, New York, 1993, p. 133.
[33] A.L. Balch, R. Koerner, L. Latos-Grażyński, J.E. Lewis, T.N. St. Claire, E.P. Zovinka, Inorg. Chem. 36 (1997) 3892.
[34] A.L. Balch, L. Latos-Grażyński, T.N. St. Claire, Inorg. Chem. 34 (1995) 1395.
[35] I. Morishima, Y. Shiro, T. Wakino, J. Am. Chem. Soc. 107 (1985) 1063.
[36] I. Morishima, H. Fujii, Y. Shiro, S. Sano, Inorg. Chem. 34 (1995) 1528.
[37] S. Sano, Y. Sugiura, Y. Maeda, S. Ogawa, I. Morishima, J. Am. Chem. Soc. 103 (1981) 2888.
[38] F.A. Walker, Coord. Chem. Rev. 186 (1999) 471.
[39] S. Sano, T. Sano, I. Morishima, Y. Shiro, Y. Maeda, Proc. Natl. Acad. Sci. USA 83 (1986) 531.
[40] A.L. Balch, R. Koerner, L. Latos-Grażyński, B.C. Noll, J. Am. Chem. Soc. 118 (1996) 2760.
[41] T.N. St. Claire, A.L. Balch, Inorg. Chem. 38 (1999) 684.
[42] A.L. Balch, L. Latos-Grażyński, B.C. Noll, M.M. Olmstead, L. Szterenberg, N. Safari, J. Am. Chem. Soc. 115 (1993) 1422.
[43] A.L. Balch, R. Koerner, M.M. Olmstead, J. Chem. Soc. Chem. Commun. (1995) 873.
[44] A.L. Balch, L. Latos-Grażyński, B.C. Noll, M.M. Olmstead, N. Safari, J. Am. Chem. Soc. 115 (1993) 9056.
[45] D.P. Hildebrand, H.-L. Tang, Y. Luo, C.L. Hunter, M. Smith, G.D. Brayer, A.G. Mauk, J. Am. Chem. Soc. 118 (1996) 12909.
[46] T. Yoshida, M. Noguchi, G. Kikuchi, S. Sano, J. Biochem. 90 (1981) 125.
[47] T. Yoshinaga, Y. Sudo, S. Sano, Biochem. J. 270 (1990) 659.
[48] A. Wilks, J. Torpey, P.R. Ortiz de Montellano, J. Biol. Chem. 269 (1994) 29553.
[49] K.M. Matera, S. Takahashi, H. Fujii, H. Zhou, K. Ishikawa, T. Yoshimura, D.L. Rousseau, T. Yoshida, M. Ikeda-Saito, J. Biol. Chem. 271 (1996) 6618.
[50] Y. Liu, P. Moënne-Loccoz, T.M. Loehr, P.R. Ortiz de Montellano, J. Biol. Chem. 272 (1997) 6909.
[51] G.C. Chu, K. Katakura, X. Zhang, T. Yoshida, M. Ikeda-Saito, J. Biol. Chem. 274 (1999) 21319.
[52] H. Sakamoto, Y. Omata, G. Palmer, M. Noguchi, J. Biol. Chem. 274 (1999) 18196.
[53] C.T. Migita, H. Fujii, K.M. Matera, S. Takahashi, H. Zhou, T. Yoshida, Biochem. Biophys. Acta 1432 (1999) 203.
[54] R.M. Davydov, T. Yoshida, M. Ikeda-Saito, B.M. Hoffman, J. Am. Chem. Soc. 121 (1999) 10656.
[55] K.E. Brancato-Buentello, W.R. Scheidt, Angew. Chem. Int. Ed. Engl. 36 (1997) 1456.
[56] W.R. Scheidt, K.E. Brancato-Buentello, H. Song, K.V. Reddy, B. Cheng, Inorg. Chem. 35 (1996) 7500.
[57] H. Song, C.A. Reed, W.R. Scheidt, J. Am. Chem. Soc. 111 (1989) 6865.
[58] W.R. Scheidt, H. Song, K.J. Haller, M.K. Safo, R.D. Orosz, C.A. Reed, P.G. Debrunner, C.E. Schulz, Inorg. Chem. 31 (1992) 939.
[59] K.E. Brancato-Buentello, S. -J. Kang, W.R. Scheidt, J. Am. Chem. Soc. 119 (1997) 2839.
[60] S.B. Brown, A.A. Chabot, E.A. Enderby, A.C.T. North, Nature 289 (1981) 93.
[61] S.B. Brown, Biochem. J. 159 (1976) 23.

[62] C.M. Gorst, A. Wilks, D.C. Yeh, P.R. Ortiz de Montellano, G.N. La Mar, J. Am. Chem. Soc. 120 (1998) 8875.
[63] D. Schuller, A. Wilks, P.R. Ortiz de Montallano, T.L. Poulos, Protein Sci. 7 (1998) 1836.
[64] G.C. Chu, S. -Y. Park, Y. Shiro, T. Yoshida, M. Ikeda-Saito, J. Struct. Biol. 126 (1999) 171.
[65] D.J. Schuller, A. Wilks, P.R. Ortiz de Montellano, T.L. Poulos, Nat. Struct. Biol. 6 (1999) 861.
[66] R. Koerner, M.M. Olmstead, A. Ozarowski, S.L. Phillips, P.M. Van Calcar, K. Winkler, A.L. Balch, J. Am. Chem. Soc. 120 (1998) 1274.